Variability, Instabilities, and Eddies in a Snowball Ocean

YOSEF ASHKENAZY

Department of Solar Energy and Environmental Physics, BIDR, Ben-Gurion University of the Negev, Midreshet Ben-Gurion, Israel

ELI TZIPERMAN

Department of Earth and Planetary Sciences, and School of Engineering and Applied Sciences, Harvard University, Cambridge, Massachusetts

(Manuscript received 29 April 2015, in final form 21 September 2015)

ABSTRACT

Oceanic variability and eddy dynamics during snowball Earth events, under a kilometer of ice and driven by a very weak geothermal heat flux, are studied using a high-resolution sector model centered at the equator, where previous studies have shown the ocean circulation to be most prominent. The solution is characterized by an energetic eddy field, equatorward-propagating zonal jets, and a strongly variable equatorial meridional overturning circulation (EMOC), on the order of tens of Sverdrups (Sv; $1\,\text{Sv} \equiv 10^6\,\text{m}^3\,\text{s}^{-1}$), restricted to be very close to the equator. The ocean is well mixed vertically by convective mixing, and horizontal mixing rates by currents and eddies are similar to present-day values. There are two main opposite-sign zonal jets near the equator that are not eddy driven, together with multiple secondary eddy-driven jets off the equator. Barotropic stability analyses, the Lorenz energy cycle (LEC), and barotropic-to-baroclinic energy conversion rates together indicate that both baroclinic and barotropic instabilities serve as eddy-generating mechanisms. The LEC shows a dominant input into the mean available potential energy (APE) by geothermal heat flux and by surface ice melting and then transformation to eddy APE, to eddy kinetic energy, and finally to mean kinetic energy via eddy–jet interaction, similarly to the present-day atmosphere and unlike the present-day ocean. The EMOC variability is due to the interaction of warm plumes driven by geothermal heating that reach the ocean surface, leading to ice-melt events that change the stratification and, therefore, the EMOC. The results presented here may be relevant to the ocean dynamics of planetary ice-covered moons such as Europa and Enceladus.

1. Introduction

"Snowball Earth" events, which are thought to have occurred at least twice during the Neoproterozoic era, between 750 and 630 million years ago (Ma), are perhaps the most dramatic climatic events in Earth's history (Harland 1964; Kirschvink 1992; Schrag and Hoffman 2001). Each event lasted millions of years, with the global mean surface atmospheric temperature dropping below −40°C and an ocean ice-cover thickness of more than 500 m (e.g., Goodman and Pierrehumbert 2003; Pollard and Kasting 2005; Goodman 2006; Tziperman et al. 2012). There is an ongoing debate regarding whether the snowball ocean was fully ice covered (Hoffman et al. 1998; Christie-Blick et al. 1999; Kennedy et al. 2001; Hoffman and Schrag 2002; Kennedy et al. 2002; Lubick 2002), yet we restrict this study to the consequences of such a thick ice cover for ocean dynamics. The oceans were not frozen to the bottom because of a geothermal heating similar to the present-day value of approximately $0.1\,\text{W}\,\text{m}^{-2}$ (Pollack et al. 1993), which is very weak relative to air–sea fluxes in a non-snowball Earth ocean. The ice and atmospheric aspects of this climate state, including challenging questions regarding its initiation and termination, have been studied in detail (see the review by Pierrehumbert et al. 2011), yet the snowball ocean has received less attention, and early works even claimed that it was stagnant under fully ice-covered conditions (Kirschvink 1992). In previous works (Ashkenazy et al. 2013, hereafter A13; Ashkenazy et al. 2014, hereafter A14), we considered the time-mean circulation of a snowball ocean under a thick ice cover, while in this paper, we discuss the strong

Corresponding author address: Yosef Ashkenazy, Department of Solar Energy and Environmental Physics, BIDR, Ben-Gurion University of the Negev, Midreshet Ben-Gurion 84990, Israel.
E-mail: ashkena@bgu.ac.il

DOI: 10.1175/JCLI-D-15-0308.1

variability of such an ocean, including eddies, eddy-driven zonal jets, and equatorial meridional overturning circulation (EMOC) variability.

Previous studies of snowball ocean that employed oceanic general circulation models (GCMs) have investigated the role of ocean dynamics in the initiation of snowball events (Poulsen et al. 2001, 2002; Poulsen and Jacob 2004; Sohl and Chandler 2007) as well as snowball dynamics when oceanic feedbacks are taken into account (e.g., Le-Hir et al. 2007; Marotzke and Botzet 2007; Abbot et al. 2011). Ferreira et al. (2011) showed, in a transient simulation of an ocean not in a steady state under 200 m of ice and without geothermal forcing, that the snowball ocean would have been well mixed and characterized by a significant equator-to-pole meridional circulation due to parameterized eddies. Yet geothermal heating at the bottom ocean was not included in the above studies, and they, therefore, could not calculate the steady-state ocean response [for geothermal effects not in the context of snowball ocean, see Adcroft et al. (2001), Scott et al. (2001), and Mashayek et al. (2013)]. Moreover, none were run at a resolution that allowed eddies and instabilities to develop (apart from a short discussion in A13), and none addressed the variability issues that are the focus of the present work.

A13 and A14 studied the combined effect of geothermal heat flux and a thick ice cover and analyzed the coupled steady ice flow and ocean circulation problem. They showed that the ocean under hard snowball conditions is highly dynamic and exhibits vigorous horizontal and meridional circulation, mainly driven by the very weak geothermal heating and, to a lesser extent, by the equator-to-pole gradient of atmospheric temperature at the top of the thick ice cover. The ocean was found to be well mixed vertically, and stratification was unstable nearly everywhere as a result of the geothermal heat flux at the bottom. The overturning circulation was strong, comparable to the present day in amplitude, yet restricted to a few degrees very near the equator. Zonal equatorial jets that are antisymmetric with respect to the equator were found, and both the EMOC and these jets were shown to be driven by weak cross-equatorial density gradients caused by the geothermal heating and by the Coriolis force. Preliminary runs at a high resolution (A13) showed a strong eddy field (comparable to the present-day ocean, although some early papers on the topic anticipated a stagnant ocean under snowball Earth conditions). A14 also performed an extensive set of sensitivity runs for the steady ocean circulation, showing the robustness of the results to many factors, including the amplitude of the geothermal heating, the spatial structure of the geothermal heating (e.g., the existence and meridional location of ridges with enhanced geothermal heating in idealized 2D latitude–depth model runs and the presence of a more realistic distribution of enhanced heating sites in tectonic spreading centers in more realistic 3D model runs), a 2D latitude–depth configuration versus a 3D configuration, the presence of realistic configuration-reconstructed continental locations, and more. The main features of the steady-state solution were found to be very robust to the model formulation.

The goals of the present paper are to 1) uncover the instability mechanisms associated with the turbulent behavior briefly reported in A13, 2) analyze the Lorenz energy cycle (LEC; Lorenz 1955; Oort and Peixoto 1983; Peixoto and Oort 1992; von Storch et al. 2012) to understand the energy sources and sinks for the snowball ocean and to better understand the underlying instability mechanisms, 3) analyze the dramatic EMOC variability seen under these conditions due to the interaction of the geothermal heating and the ice cover that has not been addressed previously, and 4) estimate the eddy mixing rates associated with this turbulent behavior.

The paper is organized as follows. We first describe the model and setup (section 2). Then we describe the results of the simulations (section 3) and discuss different instability mechanisms and the LEC for the simulated snowball ocean (section 4). Eddy viscosity and diffusion coefficients are estimated (section 5), and we end with a summary and discussion (section 6).

2. Model description

We use the Massachusetts Institute of Technology General Circulation Model (MITgcm; Marshall et al. 1997) that includes primitive equations for the ocean in a z-coordinate, free surface configuration. A longitude–latitude grid is used, with a resolution of $1/8°$, and a domain spanning 45° in the zonal direction and 42° in the meridional direction (21°S–21°N), where walls are specified at the northern and southern boundaries and periodic boundary conditions are used in the zonal direction. While computational cost does not permit a global run at this resolution, the domain used here is twice as large in the meridional direction as that used in the preliminary eddy-resolving snowball calculation of A13. The domain is restricted to the low latitudes following our previous studies (A13; A14) that indicated that ocean circulation under snowball conditions, as reflected in both zonal flow and EMOC, is more vigorous at low latitudes. We used 20 vertical ocean levels, with a uniform vertical grid separation of 100 m, spanning a total ocean depth of 2 km (one expects about 1 km of sea level equivalent of ocean water to be

deposited as ice over the continents and another 1 km or so to be frozen at the top of the ocean, leaving the remaining ocean depth at 2 km). The ocean bottom is assumed to be flat. No-slip boundary conditions were specified at the walls and the bottom of the ocean. To account for the thick sea ice cover, we used the ice-shelf package of the MITgcm (Losch 2008) and the parameter values therein; this package evaluates the heat and freshwater fluxes at the ocean–ice interface.

The ocean is forced by a bottom geothermal heating with a mean value of 0.1 W m^{-2} (Table 4 of Pollack et al. 1993). Geothermal heat flux is known to be enhanced at midocean ridges by a factor of about 4, and in order to represent this, we specify enhanced geothermal heating with a maximum value of 4 times the background value, centered at 6°N and decaying as a Gaussian meridionally {i.e., proportionate to $\exp[-(\phi - 6)^2/3^2]$, where ϕ is the latitude in degrees}; the heating field extends uniformly over all longitudes. An ice cover at the surface of a snowball ocean can deform and flow under its own weight from high latitudes, where there is net freezing and snow precipitation, to low latitudes, where there is melting at the base of the ice and net sublimation at the top of the ice (e.g., Goodman and Pierrehumbert 2003; Pollard and Kasting 2005; Goodman 2006; Li and Pierrehumbert 2011; Tziperman et al. 2012). However, because of the high computational cost of an eddy-resolving simulation, we cannot apply the coupled ice–ocean flow model used in A13 and A14, and instead we prescribe a uniform ice thickness. Moreover, the above previous studies indicate that the spatial differences in ice thickness are relatively small (around 100 m) for a wide range of forcing conditions, justifying our choice of uniform ice cover. The ice thickness is calculated to allow the geothermal heat flux (at a spatial average of 0.1 W m^{-2}) to escape, assuming an ice surface temperature of $T_{\text{surf}} = -44.43$°C and a basal freezing temperature of $T_{\text{freezing}} = -3.53$°C. The heat flux through the ice is then given by $Q = \rho_I c_{p,I} \kappa_I (T_{\text{freezing}} - T_{\text{surf}})/h$, leading to $h = 1160$ m, where $\rho_I = 920$ kg m^{-3} is the density of ice water, $c_{p,I} = 2000$ J K^{-1} kg^{-1} is the heat capacity of ice, $\kappa_I = 1.54 \times 10^{-6}$ m^2 s^{-1} is the heat diffusivity of ice, and $Q = 0.1$ W m^{-2} is the average bottom geothermal heat flux.

We use the equation of state of Jackett and McDougall (1995). The reference ocean temperature and salinity are about −3.57°C and about 49.38 ppt, respectively. For the horizontal viscosity parameterization, we use the Leith scheme (Leith 1967, 1996; Adcroft et al. 2010), which is often used in eddy-resolving simulations. The vertical viscosity coefficient is 10^{-3} m^2 s^{-1}. The horizontal diffusion coefficient for temperature and salinity is 5 m^2 s^{-1}, and the vertical diffusion coefficient is 10^{-4} m^2 s^{-1}; the vertical diffusion coefficient is relatively high compared to the typically used present-day value of 10^{-5} m^2 s^{-1} (Munk and Wunsch 1998; Wunsch and Ferrari 2004), and we test the sensitivity of our results to this parameter below. We note that the snowball ocean is vertically unstable over significant parts of the domain, and this triggers convective mixing that is much stronger than the specified vertical diffusion coefficient, making its precise value less critical. The stratification we find is exceedingly weak, and a stratification-based parameterization (Gargett 1984) would, therefore, predict a higher diffusivity. In addition, double-diffusion convection may lead to higher vertical diffusivity (Vance and Brown 2005; Vance and Goodman 2009). On the other hand, internal wave sources in a snowball ocean are restricted to tides, with no surface excitation by wind and surface waves, which implies a weaker diffusivity. The bottom line is that estimating what the mixing coefficient should be is not straightforward, and we have checked that our results are not sensitive to this choice. For convective adjustment, we use the implicit vertical diffusion of the MITgcm with a coefficient of 10 m^2 s^{-1}. In addition, advection scheme 33 of the MITgcm (third-order direct space–time flux limiter) was used (Adcroft et al. 2010). The momentum and tracers' time step is 300 s.

One expects to find most landmasses near the equator during snowball events (Kirschvink 1992; Li et al. 2008). To study the effect of land on the ocean dynamics, and in particular on the equatorial jets anticipated by the coarser-resolution runs, we accordingly prescribe, in some experiments, a circular continent at the equator whose radius is 5.5°. We refer below to this experiment as the island experiment. We have also studied the ocean circulation without the circular island (referred to below as the no-island experiment).

We integrate the model for a few hundred years until a quasi-steady state is achieved—that is, until the eddy motions and eddy kinetic energy equilibrate and the spatial means of key variables fluctuate around a constant mean value.

3. Results

a. Temperature, salinity, and EMOC

Snapshots of temperature, density, zonal velocity, and salinity from the island experiment at the upper-ocean level are shown in Fig. 1, and zonally averaged sections are shown in Fig. 2. The temperature range at this level is very small (~0.1°C), and the warmest water is found at the latitude range between the equator and approximately 10°N, near the enhanced geothermal heating region specified north of the equator (Fig. 2a). The salinity (Figs. 1d and 2d) is lowest in the area of enhanced

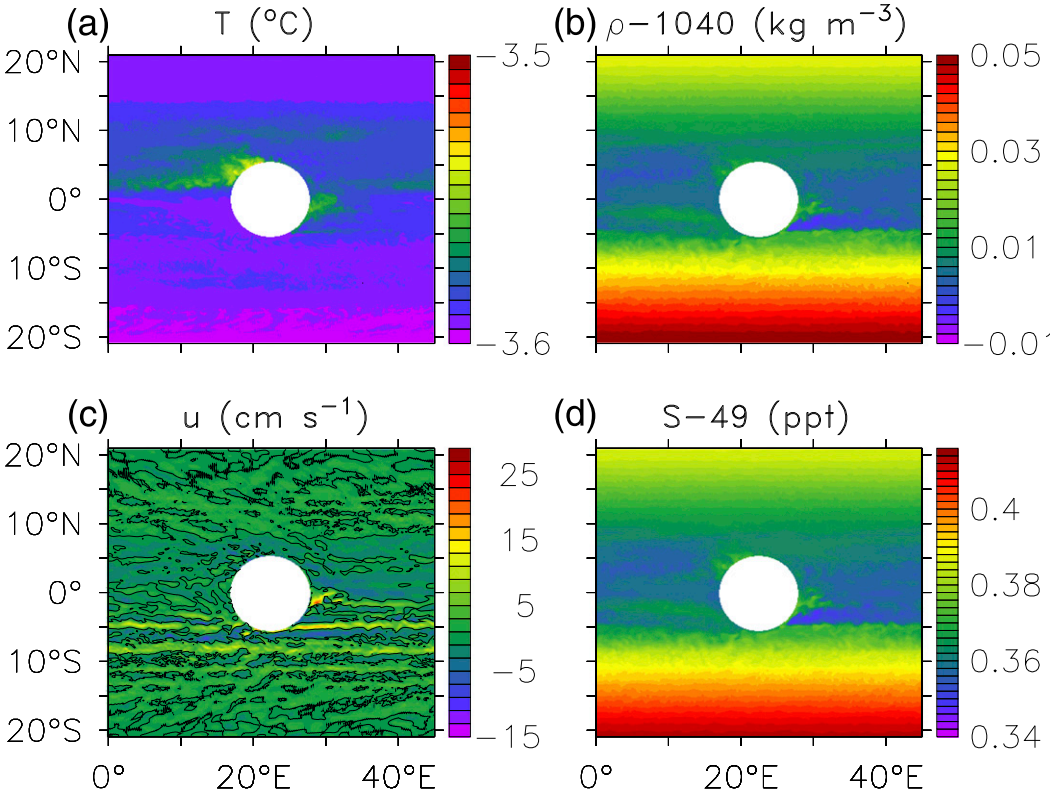

FIG. 1. Snapshots of the model solution at $t = 100$ yr showing (a) temperature (°C), (b) density (kg m^{-3}), (c) zonal velocity (cm s^{-1}), where the black contour line indicates the zero velocity, and (d) salinity (ppt, with 49 ppt subtracted) just under the ice. Note the similarity in the pattern of density and salinity, indicating that density is dominated by salinity variations.

heating because of the intensified melting caused by this heating. The density is dominated by salinity variations as can be deduced by comparing the density and salinity fields—the haline coefficient of the linearized equation of state is more than an order of magnitude larger than the thermal coefficient. The ocean temperature and salinity are vertically uniform over large areas because of convective adjustment mixing driven by geothermal heat flux, except where salinity stratification is caused by enhanced surface melting near the equator and over the enhanced heating region.

The EMOC (Fig. 3d) is strong [~20 Sv (1 Sv ≡ 10^6 m^3 s^{-1})] and is composed of a cell restricted to a few degrees near the equator. The circulation is upward north of the equator due to the enhanced geothermal heating there, although the equatorial location of the EMOC is not sensitive to the location of the heating (A14). The width of the EMOC cell is determined by the effective turbulent eddy viscosity (A13; A14) and is, therefore, sensitive to eddy motions. As the presence of the island affects the jets and eddies (see below), it also affects the EMOC, and the no-island run (not shown) yields an EMOC cell that is broken into a few small, approximately 1°–2° latitude-wide cells near the equator. The EMOC amplitude is comparable to that of the present day, in spite of the very weak forcing by geothermal heating. The overall EMOC structure was explained and the sensitivities to various parameters were thoroughly explored by A13 and A14; our focus here is on the variability.

b. *Upwelling and melting*

Ice thickness is of interest because of its role in the survival of photosynthetic life during snowball events. Melting as a result of ocean circulation has been either neglected in previous studies or calculated without considering detailed ocean dynamics (e.g., Goodman and Pierrehumbert 2003; Pollard and Kasting 2005). We find regions of enhanced melting northwest of the island (Fig. 3a, indicated by a rectangle). The maximum melting rate is even larger than that previously reported by A13, based on a smaller-domain and a shorter-integration eddy-resolving run, and is an order of magnitude larger than those previously calculated by coarser-resolution models (Goodman and Pierrehumbert 2003; Pollard and Kasting 2005; A13; A14). The maximum melting rates are

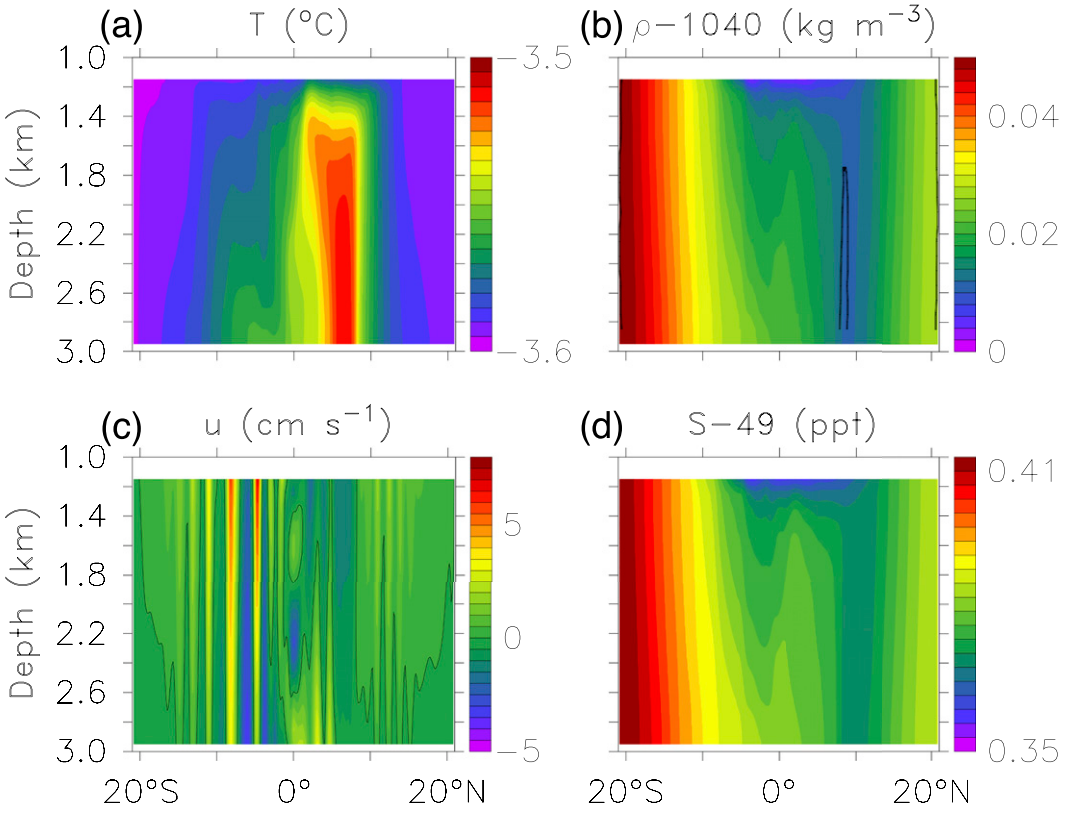

FIG. 2. Zonal average of the model solution at $t = 100$ yr of (a) temperature (°C), (b) density (kg m^{-3}), (c) zonal velocity (cm s^{-1}; the zero velocity is indicated by the contour line), and (d) salinity (ppt, with 49 ppt subtracted).

associated with warmer under-ice temperatures due to a narrow coastal warm water upwelling zone enabled by the high-resolution configuration. The ocean is salt stratified in this region as a result of the surface ice melting, and the deep ocean is warmed by the geothermal heat flux there. The upwelling of this slightly warmer deep water leads to the very high melt rates. The upwelling results from a jet flowing in the upper ocean away from the continent and an eastward jet toward the continent in the deep ocean (Fig. 3c). Because the stratification is weak, the zonal jet away from the coast can lead to upwelling rather than to a compensating alongshore horizontal circulation, and hence to the enhanced melting. A similar but smaller melting signal is seen southeast of the continent; the melt rate is much lower in other regions. While this melting rate is higher than previous estimates, an application of the model of Tziperman et al. (2012) shows that ice flow driven by the thickness gradients formed by the melting would efficiently prevent the formation of open water.

c. *EMOC variability*

Figure 4 shows time series of several variables of the island and no-island experiments. In addition to the turbulent behavior demonstrated in Fig. 1, there are irregular oscillations with a period of about 15 yr that can be seen in the temperature and salinity in the island case and of about 80 yr for the no-island case. The temperature and salinity variations are much larger for the no-island case. These oscillations are nonlinear in both cases (time series do not resemble a sine-like time dependence) and are more nonlinear for the no-island case, having a relaxation-oscillation character (gradual evolution terminated by an abrupt change).

Figures 4a,b show time series of maximum EMOC (between 5°S and 5°N) for the island and no-island experiments. The variations in the maximum EMOC in the island experiments are relatively small, around a mean value of approximately 22 Sv. Those of the no-island experiment are much larger (EMOC ranges from 10 to 60 Sv), have the character of a relaxation oscillation, and result from a combination of temperature increase due to geothermal heating and salinity response to surface ice-melt events, as follows. The bottom geothermal heating leads to a gradually increasing deep temperature that is carried by mixing and advection toward the surface on a time scale of a few decades. At the same time, the salinity in the upper ocean, just under the ice,

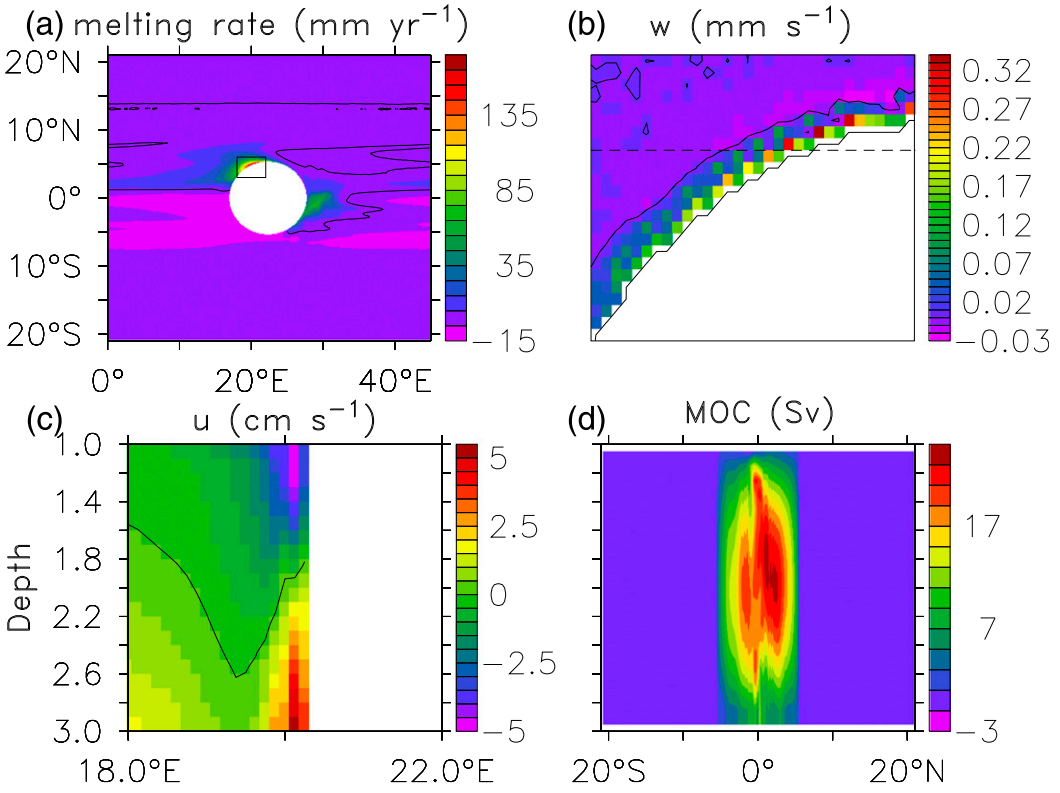

FIG. 3. (a) Melting rate of the ice cover (mm yr^{-1}), (b) vertical velocity (mm s^{-1}) of the region of enhanced melting indicated by the black rectangle in (a), (c) zonal cross section at 5°N of the zonal velocity (cm s^{-1}) in the region of enhanced melting, along the dashed line shown in (b), and (d) the meridional overturning circulation (Sv). The black contour line indicates a zero value. In all panels, a temporal mean over 240 years of simulation is shown.

increases as a result of advection and mixing from below and from the south. The gradual northward protrusion of salty water lasts until just before the melt event, as can be seen in Figs. 5a,c, which show latitude–depth temperature and salinity sections at year 70, just before the melt event. The salinity increase is also seen in the time–latitude plot of salinity under the ice in Fig. 6b. At some point, the surface salinity increase weakens the stratification sufficiently to allow the subsurface warm water to reach the ice. The resulting warm water protrusions are seen as red dots in the time–latitude plot of ocean temperature just under the ice of Fig. 6d at years 80 and 160, north of the equator. The warm water reaching the ice induces a strong melt pulse, leading to the freshwater cap seen in the latitude–depth salinity plot representing year 84 in Fig. 5b, and in the latitude–time salinity plot in Fig. 6b. This freshwater cap leads to a renewed salt stratification, keeps the warm water away from the ice, and shuts off the melt event, restarting the process. The horizontal salinity gradients developing and vanishing as a result of this cycle affect the meridional pressure gradient across the equator and, therefore, lead to changes in the EMOC (A13; A14) and in the jets, which are also reflected in the total kinetic energy (Fig. 4). The zonally averaged zonal jets dominate the kinetic energy (black lines in Figs. 4b,d) and contribute more than the eddies (red lines). As expected, owing to the barrier effect of the island, the kinetic energy of the no-island experiment is about 4–10 times larger than that of the island case.

d. Jets

The flow throughout the domain is vigorous and turbulent. Zonal jets are found throughout the domain (Fig. 1c) and fall into two categories. First is the equatorial jets, which change sign with depth (Fig. 2c), as in the coarser-resolution simulations of A13 and A14. These baroclinic jets occur because of a combination of a cross-equatorial pressure gradient and the Coriolis force near the equator, and their structure was explained via an analytic argument in the above papers. Second, the jets at higher latitudes are eddy driven, as seen by the overlap of jet location and the convergence of meridional eddy momentum flux $[-(\overline{u'v'})_y$; Fig. 7]. The eddies leading to this flux depend, in turn, on the instability of the jets as discussed in section 4 below. These jets are

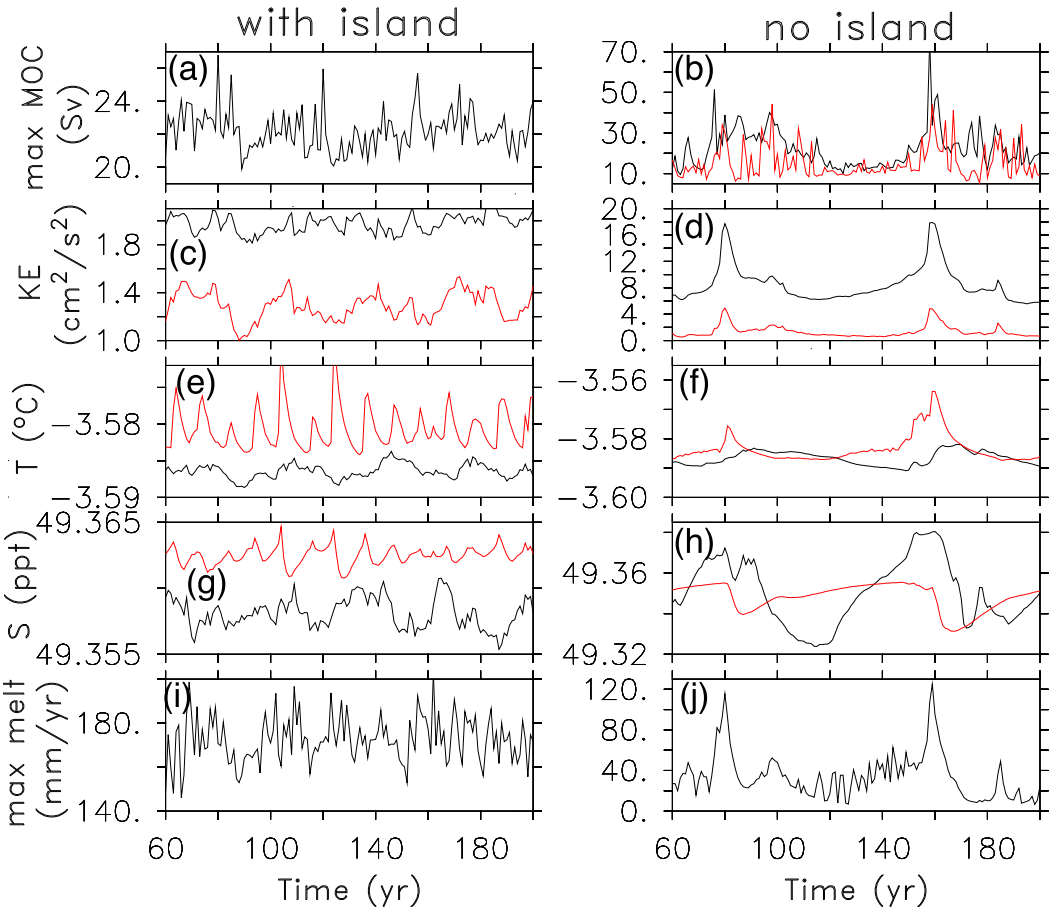

FIG. 4. Time series of different variables related to the EMOC oscillations for the (left) island and (right) no-island experiments. (a),(b) Maximum EMOC time series (between 5°S and 5°N). The EMOC in the no-island case is broken into several narrow cells, and we therefore plot both the anticlockwise circulation (black) and clockwise circulation (red) in (b). (c),(d) Kinetic energy based on the total velocities (black) and on the eddy deviations from the zonal-mean velocities (red). (e),(f) Temperature at 3°S (black) and 8°N (red) at the second-from-top level of the ocean. (g),(h) Salinity at 3°S (black) and 8°N (red) at the second-from-top level of the ocean. (i),(j) Maximum ice-melting rate.

most clearly seen just south of the island (Figs. 1c and 2c). A typical jet's speed is about 10 cm s^{-1}, and its magnitude decays away from the equator (justifying our choice of an equatorial sector rather than an off-equatorial sector). These jets are quite narrow, spanning about 1° latitude. The two equatorial jets (especially in the no-island run) do not coincide with the eddy momentum flux divergence (which vanishes near the equator), consistent with the observation that they are not eddy driven.

The jets are not stationary in these runs, and both the island and no-island runs show them to be migrating equatorward, mostly in the Southern Hemisphere (Fig. 8). Both the zonal-mean zonal velocity and the eddy momentum flux divergence exhibit this equatorward migration. Similar equatorward jet migration was reported by Chan et al. (2007), who suggested a mechanism based on an eddy-driven secondary circulation acting on the temperature field. A poleward jet migration was observed in the atmospheric simulations of Chemke and Kaspi (2015) and was suggested to be due to eddy momentum fluxes acting differentially on the two sides of the jet. A close look at Fig. 7 suggests that the peaks of the eddy momentum flux convergence as a function of latitude are shifted equatorward relative to the peaks of the zonal velocity, especially for the most equatorward eddy-driven jet at about 5°S, indicating that the eddies act to shift the mean flow, similar to the analysis of Chemke and Kaspi (2015). A more complete explanation of the equatorward jet migration would require further study.

e. *Sensitivity tests*

The introduction summarizes the extensive set of sensitivity simulations performed for the steady state by A14. The higher computational cost of the eddy-resolving

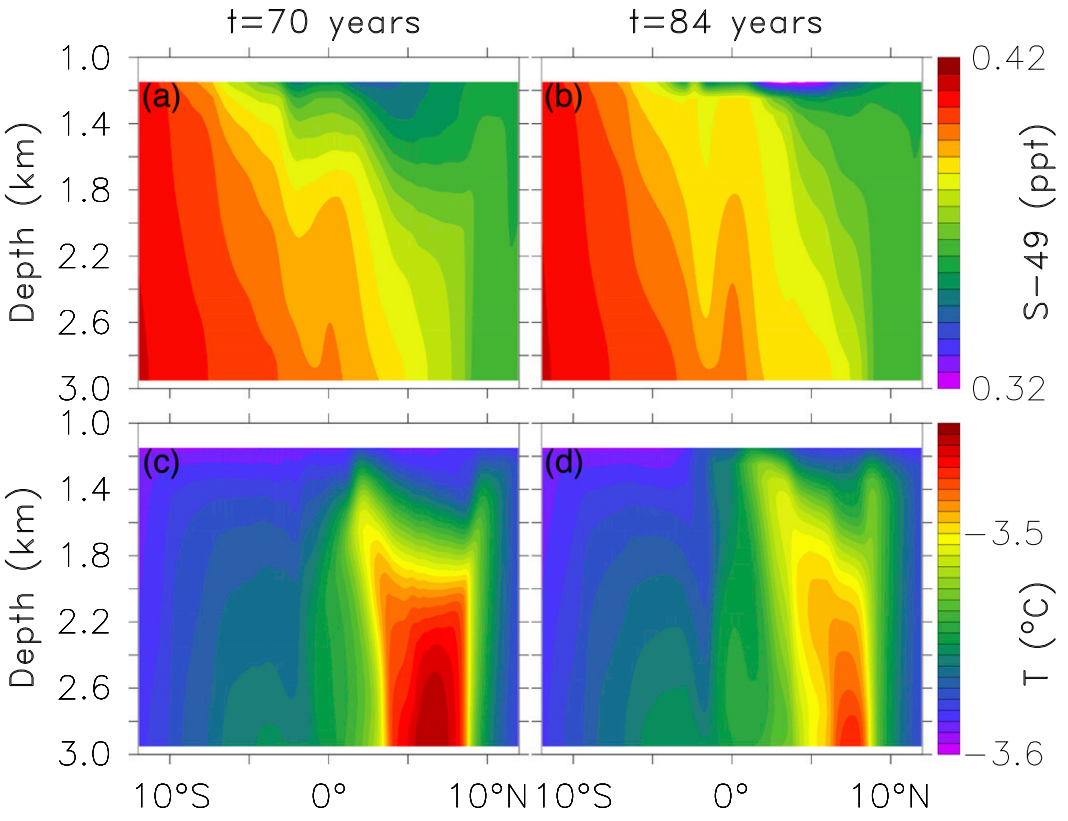

FIG. 5. Zonal-mean (a),(b) salinity and (c),(d) temperature for the no-island experiment (left) prior to and (right) after the peak of a relaxation oscillation.

runs considered here allows a smaller set of sensitivity tests that are briefly described below, and these again demonstrate the robustness of our results to the model configuration. Specifically, the main EMOC cell, the zonal jets, and the strong eddy field and variability were common to all the sensitivity runs. In addition, enhanced melting regions were common to all the island experiments, while the relaxation oscillations were common to almost all the no-island experiments. Each sensitivity case described below was integrated on the order of 100 years (starting from the steady-state solutions of the island and no-island runs presented above), allowing for an equilibration of the kinetic energy and jets.

1) The big-island run is similar to the island run but with a radius that is 2 times larger, which more effectively blocks the zonal jets and reduces the kinetic energy by a factor of 2. Yet, the enhanced melting regions are still at the northwest and southeast sides of the island. The zonal jets and their migration were similar to the island run.
2) The island run with weak vertical diffusion reduces the vertical diffusion coefficient from 10^{-4} to $10^{-5}\,m^2\,s^{-1}$, the typically used value for present-day simulations (Ledwell et al. 1993; Munk and Wunsch 1998; Wunsch and Ferrari 2004). The kinetic energy is reduced by about 15%. The enhanced melting can still be found on the southeastern side of the island, while the northwestern enhanced melting region is shifted to the northern side of the island. Zonal jet migration persists, yet it is slower.
3) For the no-island run with weak vertical diffusion of $10^{-5}\,m^2\,s^{-1}$, the kinetic energy is reduced by a factor of 2, and the flow pattern combines turbulent eddies, as in our standard cases, and wave motions resembling present-day tropical instability waves seen in the SST. Multiple equatorially migrating jets are still found. The relaxation oscillations (Fig. 4d) are not seen, possibly because the time it takes for the warm plumes to diffuse up to the ice surface has been extended by the weaker vertical diffusion to beyond our model's run duration.
4) For the island run with geothermal heating centered at 12°N instead of at 6°N, the kinetic energy is weaker by about 15%, and the higher-temperature and low-salinity regions are shifted to 12°N. The EMOC cell is still at the equator, and equatorward-migrating jets

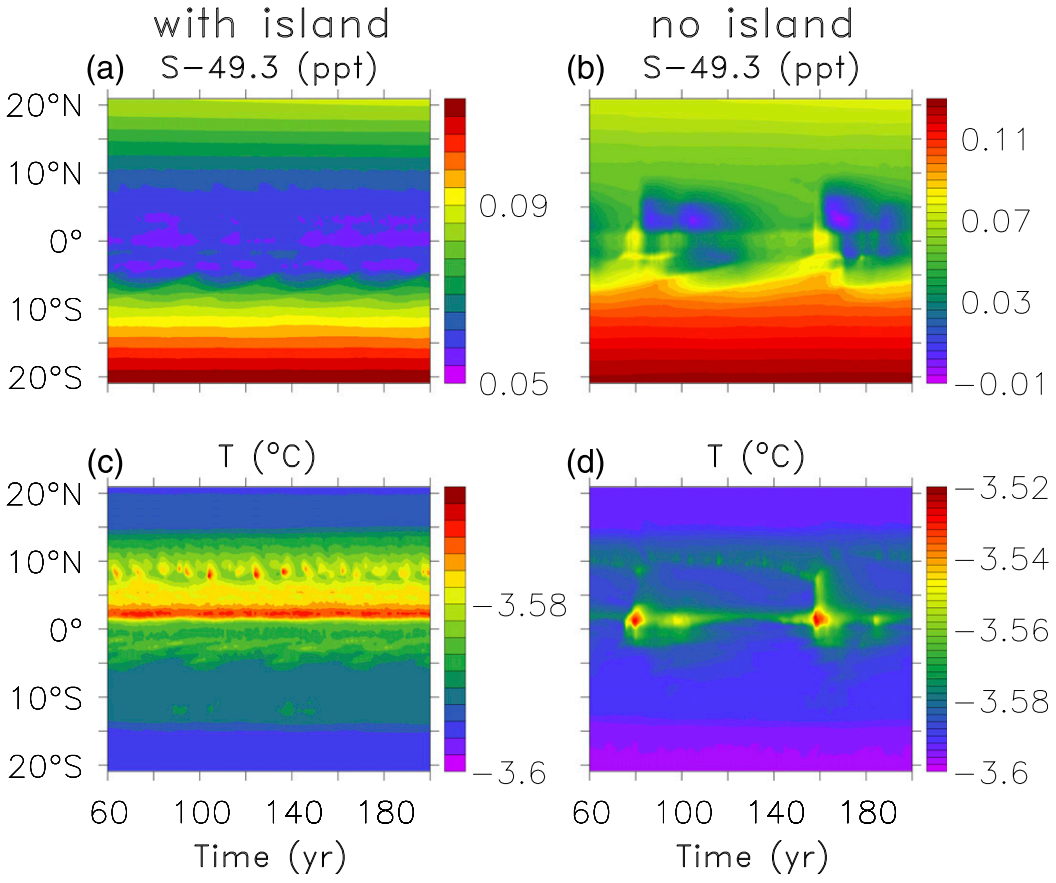

FIG. 6. Time–latitude plots of zonally averaged (a),(b) salinity and (c),(d) temperature just under the ice, for the (left) island and (right) no-island experiments. The warm water penetration toward the surface, leading to the strong melt events and EMOC oscillations, is seen by the red spots in (d).

are observed in this case even poleward of 15°S and 15°N. Enhanced melting regions are as in the island run.

5) For the no-island run with geothermal heating centered at 12°N instead of at 6°N, the kinetic energy is weaker by about 20% in this experiment, and the relaxation oscillations were still present. At the bottom of the ocean, the region of high temperature and low salinity was shifted northward from 6°N toward the location of the enhanced bottom heating, 12°N. The EMOC, the jets, and their variability were not affected.

Using spatially uniform geothermal heating in the non-eddy-resolving case of A14 still allowed for a significant yet weakened EMOC, while additionally eliminating the meridional atmospheric temperature gradient led to the vanishing of the circulation. In the present eddy-resolving case, given that the atmospheric temperature is prescribed to be uniform, turning off the enhanced heating region leads to a weakening tendency of the circulation, consistent with A14, yet we have not obtained the steady-state solution in this case.

4. Instability and eddy-generation mechanisms

We now address the eddy-generation instability mechanisms leading to the turbulent flows described above. The necessary conditions for inertial instability and symmetric instability are not satisfied for our numerical experiments poleward of 1°N and 1°S, and therefore, we next consider barotropic instability (section 4a) and the LEC (section 4b).

a. Barotropic instability

We start by calculating an upper bound for the viscosity coefficient, below which barotropic instability may occur, based on the analytic expression for the equatorial region zonal velocity derived in A14:

$$u = \frac{g\beta\rho_y(z+H/2)}{40\rho_0\nu_h^2}\left(\frac{y^5}{y_0^5} - 3\frac{y^3}{y_0^3} + 3\frac{y}{y_0}\right)y_0^5, \qquad (1)$$

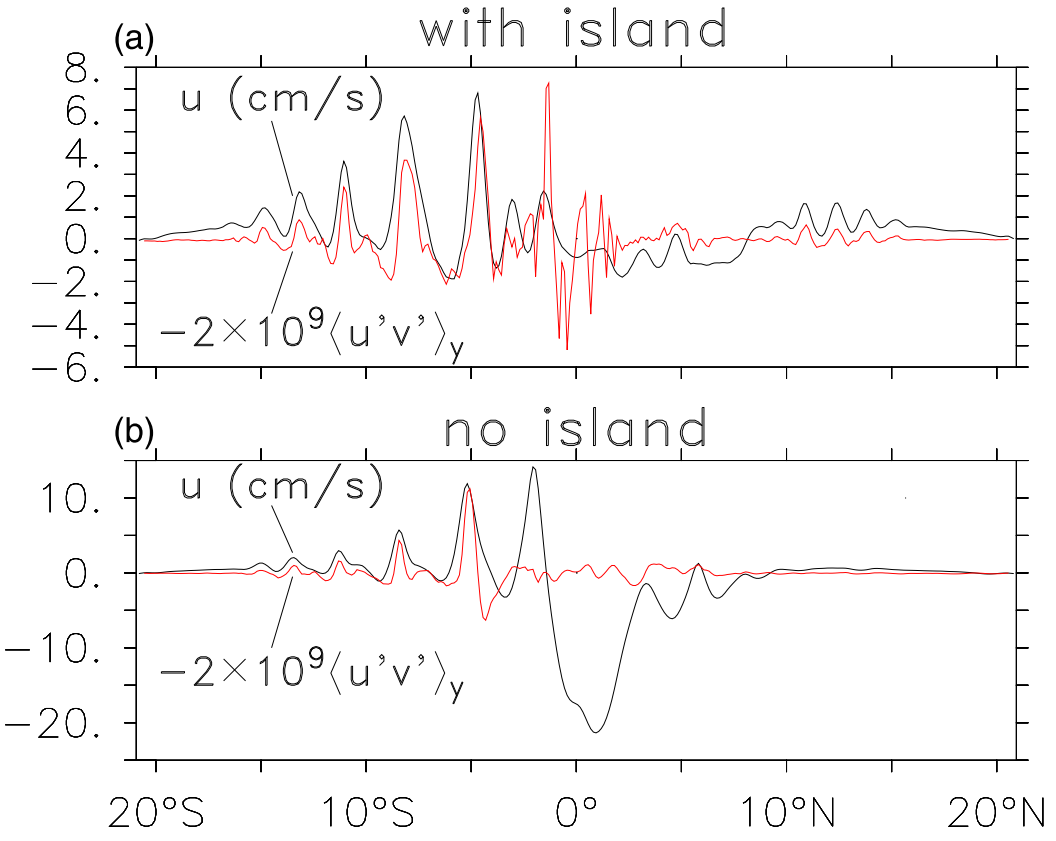

FIG. 7. Zonal-mean zonal velocity (black) and eddy momentum flux divergent (red) just under the ice, as a function of latitude at $t = 100$ yr for the (a) island and (b) no-island runs.

where g is the gravitational acceleration; $\beta = df/dy|_{f=0}$, with f the Coriolis parameter; ρ_0 is the mean ocean density; ρ_y is the density gradient across the equator, which is assumed constant; ν_h is the horizontal viscosity coefficient; and $y_0 = 40^{1/6}(\nu_h/\beta)^{1/3}$ is a length scale on the order of 100 km that characterizes the meridional extent of the equatorial jets and is similar to the scale of the half-width of the EMOC. The above expression shows a change from zero at the equator to an extremum at points north and south of the equator, then decaying poleward. Based on the second derivative of this expression, we look for the viscosity ν_h for which $\beta - u_{yy}$ changes sign as a function of latitude, allowing barotropic instability to develop, and we find that this condition is satisfied when

$$\nu_h \leq \frac{3\sqrt{3}g\rho_y H}{10\rho_0\beta}, \tag{2}$$

where $H = 2$ km is the ocean depth. For a typical value of $\rho_y/\rho_0 = 2 \times 10^{-12}\,\mathrm{m}^{-1}$ in our runs, we obtain an estimate for the eddy viscosity coefficient, below which one expects barotropic instability to occur (i.e., $\nu_h < 1000\,\mathrm{m}^2\,\mathrm{s}^{-1}$). The global mean eddy diffusion coefficients are estimated later (section 5) to be 1700 and 760 $\mathrm{m}^2\,\mathrm{s}^{-1}$ for the island and no-island experiments, respectively. These values are sufficiently close to the stability threshold to suggest that the snowball circulation may be brought by the eddy-mean flow interaction to near a marginally stable state, as is often claimed to be the case for the present-day ocean and atmosphere (e.g., Farrell and Ioannou 1995; Jansen and Ferrari 2012).

To further analyze the possible occurrence of barotropic instability, we numerically solved the Rayleigh equation (Vallis 2006):

$$(u - c)(\psi_{yy} - k^2\psi) + (\beta - u_{yy})\psi = 0, \tag{3}$$

where u is the zonal mean of the zonal current in our GCM solutions at different vertical levels and for the instantaneous velocity at different times, and $\exp[ik(x - ct)]\psi(y)$ is the streamfunction.

Figure 9 shows the results based on the velocity at the second-from-top vertical level, just under the ice. Figures 9a,b show that while $\beta - u_{yy}$ is generally positive in our simulation, it changes sign around the jets at the times and locations indicated by color pixels. The

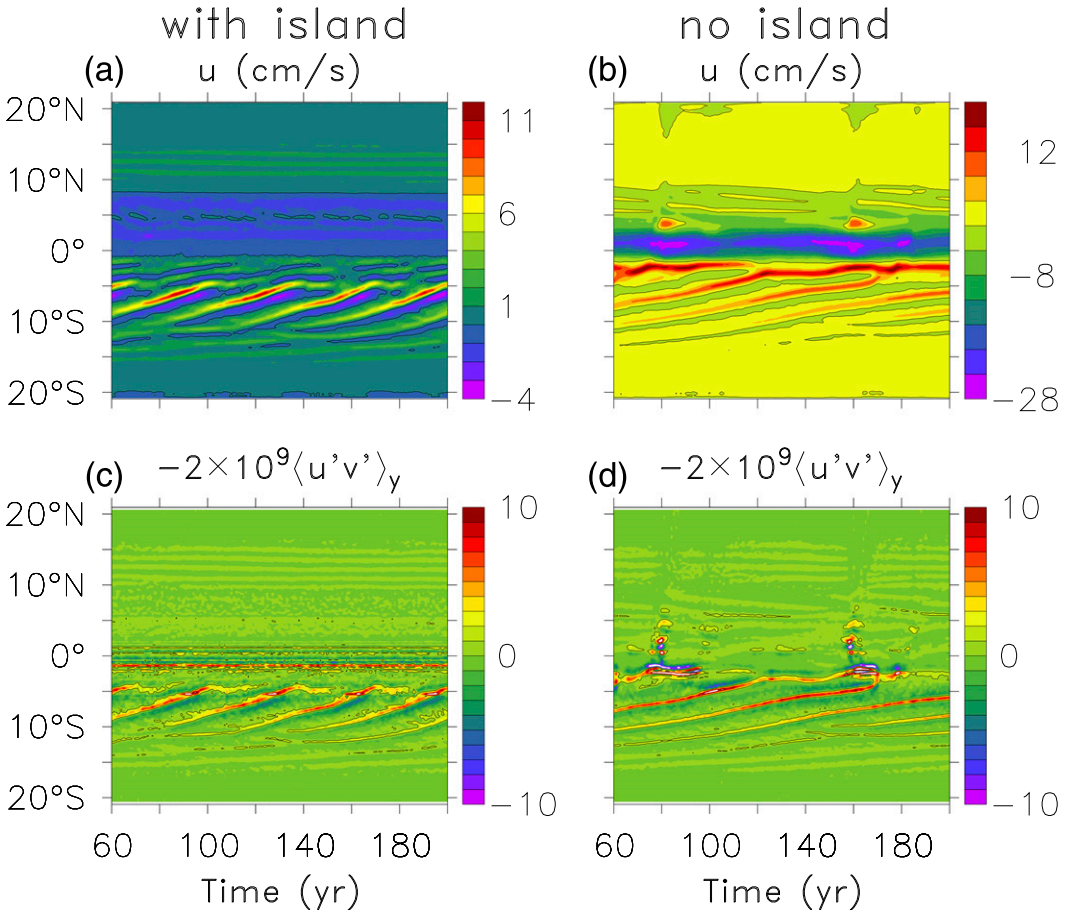

FIG. 8. Zonal-mean (a),(b) zonal velocity and (c),(d) eddy momentum flux convergence just under the ice as a function of latitude and time, for the (left) island and (right) no-island runs.

jets are not completely depth independent, and when this analysis is performed at each model level, the number of grid points with negative $\beta - u_{yy}$ is largest just under the ice where the velocities are strongest. The barotropic instability is also stronger for the no-island experiment, since the jets are not blocked by the landmass, are more vigorous, and lead to a stronger eddy field.

In Figs. 9c,d, we present the growth rate versus wavenumber for $t = 100$ yr. The maximum growth rate for the island experiment for this time is $1/508\,\text{day}^{-1}$ obtained for $k = 0.027\,\text{km}^{-1}$ (230-km wavelength). The temporal mean of the maximum growth rate is $1/136\,\text{day}^{-1}$, and the mean corresponding wavenumber is $0.028\,\text{km}^{-1}$. In the no-island experiment, the growth rate at $t = 100$ yr is $1/278\,\text{day}^{-1}$ obtained for $k = 0.02\,\text{km}^{-1}$ (313-km wavelength). The temporal mean of the maximum growth rate is $1/88\,\text{day}^{-1}$, and the mean corresponding wavenumber is $0.024\,\text{km}^{-1}$.

These time and length scales are not incompatible with the eddies observed in the numerical simulation, suggesting that barotropic instability is a relevant eddy-generation mechanism in these runs. The eigenfunction $\psi(y)$ corresponding to the eigenvalue of phase speed c, which leads to maximal growth rate, strongly peaks at Southern Hemisphere latitudes where $\beta - u_{yy}$ changes sign and where the jets are stronger, indicating the location of eddy generation by this mechanism. We will show in the following that while barotropic instability seems to be an active source of eddy kinetic energy, the net flow of kinetic energy is from eddies to the mean, via eddy-mean flow interactions.

The above Rayleigh equation analysis is performed on the instantaneous flow. An alternative would have been to perform it on the smoother time-mean flows, and it is then customarily consistent to include in the Rayleigh equation a term representing the effect of these eddies, perhaps in the form of an enhanced turbulent viscosity. However, eddy viscosity does not represent the up-gradient momentum fluxes of the eddies, and we avoided this issue by analyzing the instantaneous flow, such

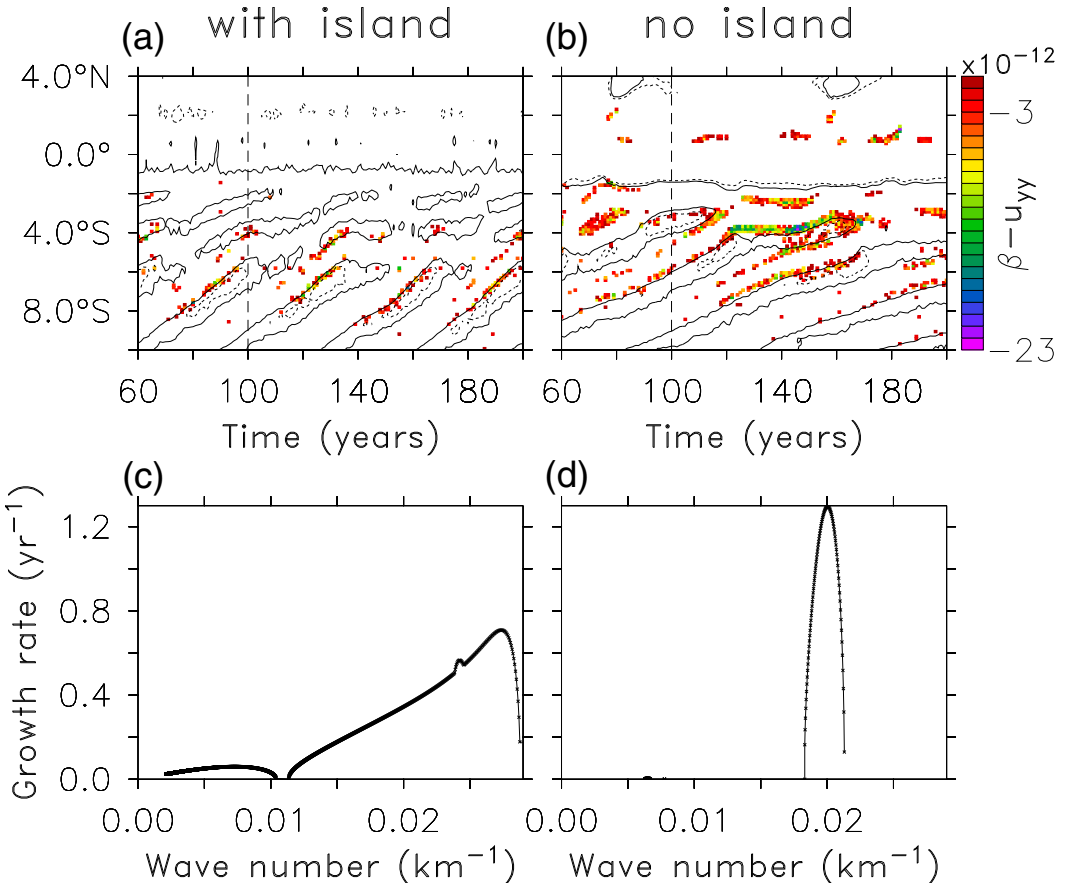

FIG. 9. Negative $\beta - u_{yy}$ are shown by the color pixels for the (a) island and (b) no-island experiments. The zero value of the zonal-mean zonal velocity is shown by the solid contour, with dashed contours indicating the location of negative values. (c),(d) The barotropic instability growth rate (yr^{-1}) vs wavenumber (km^{-1}) for the island and no-island experiments calculated by solving Eq. (3) for the zonal-mean model velocity at the top model level under the ice at $t = 100$ yr [this is the time indicated by the dashed vertical lines in (a) and (b)].

that the dissipation appearing in this equation needs to be the one used in the model, rather than an estimate of the eddy viscosity. Our model uses a nonlinear Leith viscosity whose value is chosen to be small, allowing eddies to develop; leaving it out should not affect the stability results significantly.

b. *The LEC and eddy-generation mechanisms*

At least one of the necessary conditions for baroclinic instability is satisfied away from the equator where u_z has the same sign at the upper and lower boundaries (e.g., Vallis 2006). It is possible to obtain a rough estimate for the characteristics of the baroclinic instability by using scales for the most unstable wavelength, depth scale, and growth rate (Vallis 2006). However, these are unreliable close to the equator. Instead, we calculate the LEC (Lorenz 1955; Oort and Peixoto 1983; Peixoto and Oort 1992; von Storch et al. 2012) that quantifies the conversions between mean flow and eddies, of both the available potential energy (APE) and kinetic energy; see appendix A for details.

The LEC diagram based on a 160-yr model integration, amounting to two EMOC oscillations of the no-island run, is shown in Fig. 10. When making comparisons with the present-day ocean, we scale our results (Fig. 10) by the volume ratio between our regional equatorial domain and the global present-day ocean volume (a factor of ~30). This is intended to allow a more meaningful comparison with the total energy conversions in the present-day ocean, yet it also introduces two issues that are important to keep in mind: 1) the global snowball ocean is only half the volume of the modern ocean, and 2) the equatorial domain we simulate, with its multiple jets, is likely more energetic than the high-latitude snowball ocean. One also wonders about the validity of the APE concept when much of the ocean is characterized by nearly vertically uniform temperature and salinity, but a back-of-the-envelope

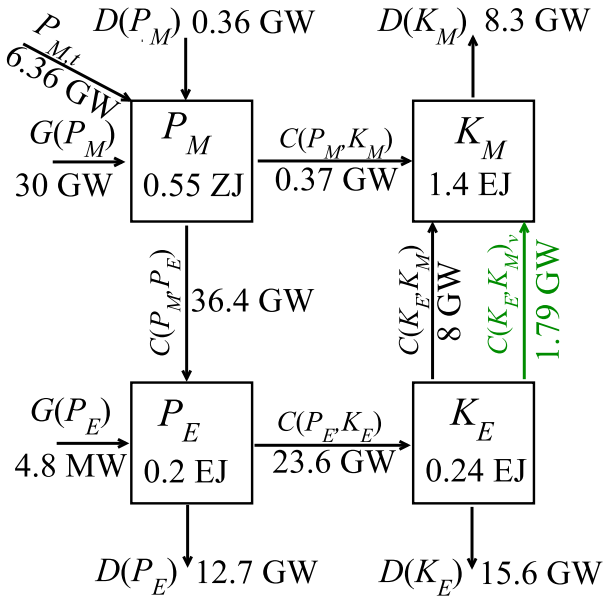

FIG. 10. LEC diagram for the no-island run. Energies are given in zettajoules (1 ZJ = 10^{21} J) and exajoules (1 EJ = 10^{18} J), while the source, conversion, and dissipation terms are given in gigawatts (1 GW = 10^9 W) and megawatts (1 MW = 10^6 W). The vertical component of the conversion between the kinetic energy of the eddies and the mean flow $C(K_E, K_M)_v$ is shown in green. Note that the time rate of change of the mean potential energy $(P_M)_t$ is included in the budget as it is not negligible. The results were multiplied by the ratio of the present-day ocean volume and the equatorial sector ocean volume considered here (29.83) to allow an easier comparison with the present-day LEC given (e.g., von Storch et al. 2012).

calculation demonstrates that the approximation is still useful (appendix C).

The mean APE P_M is much larger than other energy components, as in the present-day ocean (von Storch et al. 2012). However, the present-day mean APE is much larger than that of the snowball ocean simulation, as a result of the small range of temperature and salinity values and, thus, the weak spatial variability of the snowball ocean's stratification. The mean kinetic energy K_M is comparable to that of the present day, while the eddy potential and kinetic energy are about one order of magnitude smaller than those of the present-day ocean; this difference is attributed to the wind source of kinetic energy that is relevant in the present-day ocean but not in the snowball ocean.

The only significant external source of energy in the snowball ocean is $G(P_M)$, the source of P_M. It is the sum of three contributions [Eq. (A12)]: heat flux through the ice at the top of the ocean, geothermal heat flux at the bottom, and ice melting and freezing at the top. The first source is found to be negligible while the other two are comparable. Tides may be an important energy source in a snowball ocean but could not be taken into account given that our model runs do not resolve tides. The P_M is transferred to eddy APE P_E, while dissipation and energy transfer to the mean kinetic energy are negligible. The P_E is transferred into the eddy kinetic energy K_E, which is then transferred into K_M. Thus, the main energy path is $P_M \rightarrow P_E \rightarrow K_E \rightarrow K_M$, unlike the present-day ocean (see von Storch et al. 2012) where there are strong external sources of both mean and eddy kinetic energy and where the equivalent path is $P_M \rightarrow P_E \rightarrow K_E$ and $K_M \rightarrow K_E$. The above energy transformation path of a snowball ocean shown in Fig. 10 is reminiscent of that of the present-day atmosphere (Li et al. 2007; von Storch et al. 2012).

The LEC provides useful information regarding eddy energy generation by baroclinic and barotropic instabilities. Energy conversion from mean potential to eddy potential energy [$C(P_M, P_E)$; Eq. (A11)] and the vertical component of transformation between the eddy kinetic and mean kinetic energy [$C(K_E, K_M)_v$; Eq. (A15)], which is mostly negligible in the present-day ocean according to quasi geostrophy, are related to baroclinic instability. The horizontal component of the transformation between the eddy kinetic and mean kinetic energy [$C(K_E, K_M)_h$; Eq. (A14)] may be due to either barotropic instability or eddy–jet flow interaction transferring kinetic energy from eddies to the mean flow. The latter is dominant in our runs, as the kinetic energy flow is from K_E to K_M (Rhines 1979; Farrell and Ioannou 2003). For the snowball ocean no-island run, the baroclinic conversion is $C(P_M, P_E) + C(K_E, K_M)_v = 38.2$ GW, while the barotropic conversion is $C(K_E, K_M)_h = 6.2$ GW. This ratio of baroclinic to barotropic conversions is similar to that of the present-day ocean (von Storch et al. 2012) and atmosphere (Li et al. 2007).

To gain insight into the latitudes at which the baroclinic and barotropic instabilities are dominant, we plotted in Fig. 11a the latitudinal dependence of $C(P_M, P_E)$, $C(K_E, K_M)_h$, and $C(K_E, K_M)_v$. These three energy conversion terms are near zero close to the equator (about 3°S–3°N, the region of the two equatorial jets), as is the eddy momentum flux convergence there (Fig. 7). Between 7°S and 7°N (except close to the equator), both $C(P_M, P_E)$ and $C(K_E, K_M)_h$ are dominant. For latitudes outside 7°S–7°N, the only dominant conversion term is $C(P_M, P_E)$, indicating that baroclinic instability dominates there. This conversion term is composed of horizontal and vertical terms [Eq. (A11)]. While quasigeostrophic theory predicts the vertical term of $C(P_M, P_E)$ to be much smaller than the horizontal one, we find them to be comparable and canceling each other out to a significant degree between 7°N and 7°S (not shown). Outside of this latitude range, the horizontal conversion term of

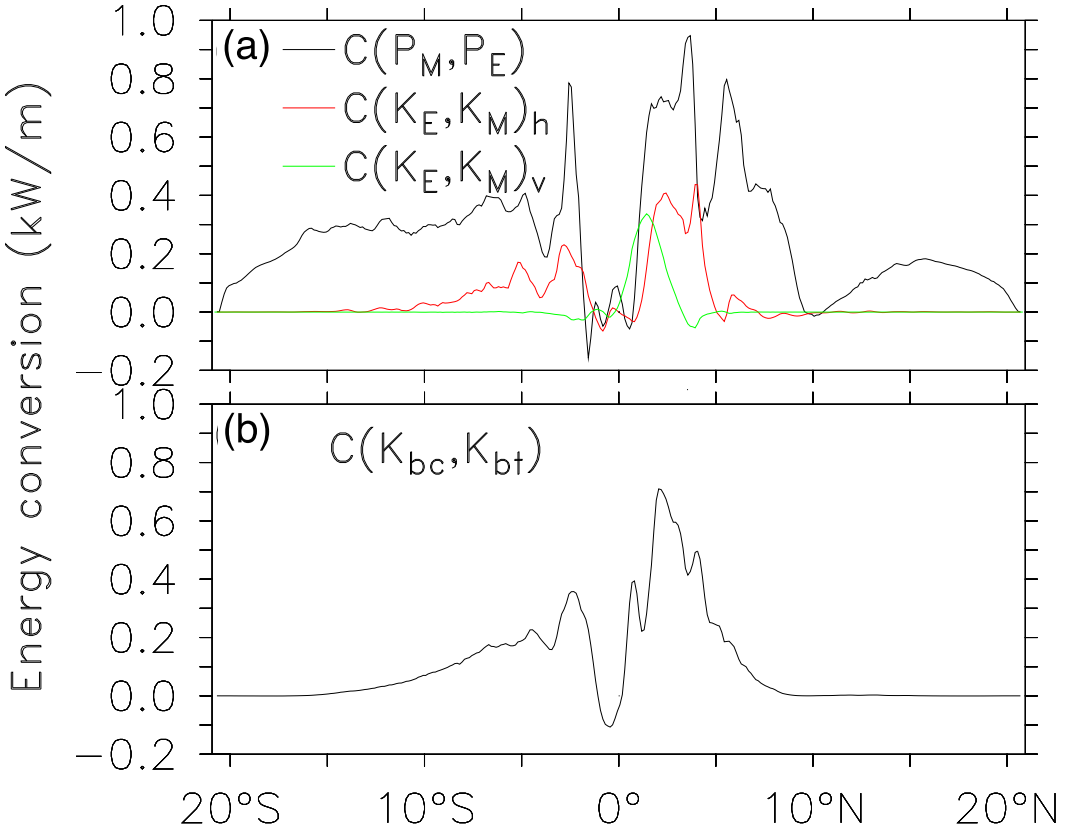

FIG. 11. (a) The latitudinal structure of the energy conversion rates $C(P_M, P_E)$ and $C(K_E, K_M)_v$, which are associated with baroclinic instability, and of $C(K_E, K_M)_h$, which is associated with barotropic instability and eddy-mean jet interactions. Baroclinic instability dominates away from the equator. (b) The conversion between the barotropic and baroclinic modes, showing that the energy transfer is from the baroclinic mode to the barotropic mode except close to the equator.

$C(P_M, P_E)$ is different from zero in the range 15°S–10°N, which is also where zonal jets persist, suggesting that these jets are again baroclinically unstable.

Poleward of 15°S and 15°N, the vertical conversion term of $C(P_M, P_E)$ dominates, yet its interpretation as being related to baroclinic instability may not be justified given that the ocean is hardly stratified there (Fig. 2). The dominance of $C(P_M, P_E)$ at the high latitudes is partly due to the absence of stratification in these regions [i.e., $\overline{\rho}_z(y, z) \to 0$], increasing P_M [Eq. (A2)] and $C(P_M, P_E)$ [Eq. (A11)]. Similarly, the weak stratification at the bottom of the ocean ($\overline{\rho}_z/\rho_0 \approx -1.8 \times 10^{-9}\,\mathrm{m}^{-1}$), both at present and in the snowball ocean, implies that even a small geothermal heat flux significantly affects the APE because of the division by small $\overline{\rho}_z$ [Eq. (A12); Huang 1999; Mashayek et al. 2013].

Finally, the energy transformation between barotropic and baroclinic modes $C(K_{\mathrm{bc}}, K_{\mathrm{bt}})$ can be calculated by evaluating the kinetic energy of the vertically averaged flow (barotropic mode) and the kinetic energy of the deviation from the vertical mean (which we refer to as the baroclinic mode) as shown in Eqs. (B3)–(B5) of appendix B. Figure 11b shows that $C(K_{\mathrm{bc}}, K_{\mathrm{bt}})$ is almost always positive, indicating a transfer from baroclinic to barotropic energy. This is consistent with (yet distinct from) the flux from P_E to K_E seen above. The transformation direction is reversed at the equator. As expected, $C(K_{\mathrm{bc}}, K_{\mathrm{bt}}) \to 0$ for the higher latitudes, where the flow vanishes.

Overall, the above analyses of barotropic instability, the LEC, and the baroclinic-to-barotropic transformation rates indicate that baroclinic instability, barotropic instability, and eddy-mean jet interactions all play an important role in the eddy dynamics of the simulated snowball ocean.

5. Estimating eddy diffusion and eddy viscosity coefficients

The eddy viscosity has been shown by A13 and A14 to determine the width of the EMOC cell near the equator, and estimates of the snowball ocean's eddy diffusivity

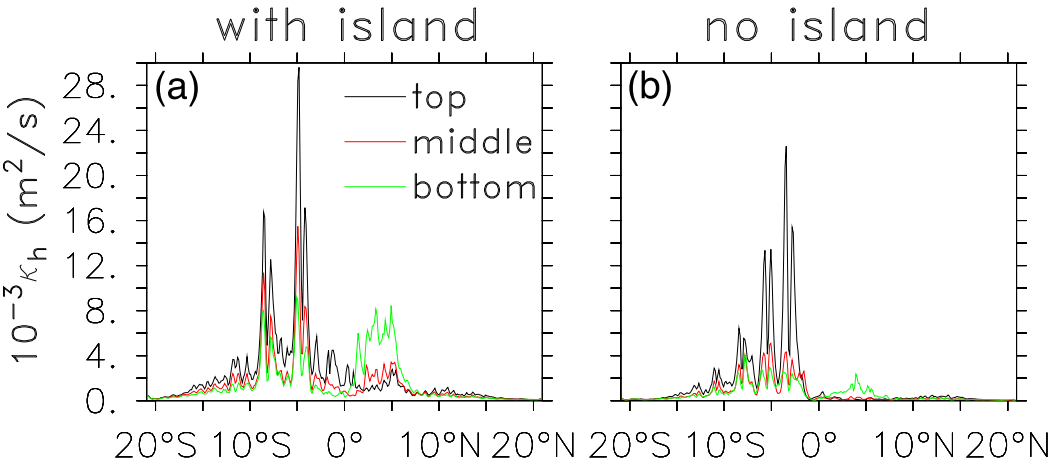

FIG. 12. Estimated horizontal eddy–parameterized diffusion coefficient for the (a) island and (b) no-island experiments. Shown are the zonal-mean coefficients vs latitudes at the top (black), middle (red), and bottom (green) of the ocean.

can help verify those theoretical estimates using the current eddy-resolving runs. Eddy coefficients may also be used to quantify mixing time scales in a snowball ocean for a comparison with the present-day ocean and potentially for interpreting geochemical observations that may require such information in the future. We estimate these coefficients based on the eddy-resolving runs presented above using the procedure described in Lemmin (1989). The horizontal diffusion coefficient can be estimated following Hinze (1975):

$$\kappa_h = \overline{u_L'^2} \int_0^\infty R(\tau)\, d\tau, \tag{4}$$

where the overbar indicates the temporal mean and the prime the anomaly from this mean and where $R(\tau) = \overline{u_L'(t)u_L'(t+\tau)}/\overline{u_L'^2(t)}$ is the autocorrelation function of the Lagrangian anomaly velocity u_L' at a time lag τ. When using the Eulerian flow instead, as we do here, one needs to multiply the above estimate by a factor γ, where we use $\gamma = 4$ following Lemmin (1989). In our analysis, $R(\tau)$ exhibits oscillations and the integral converged in some locations to negative values, and these locations were excluded. We assume that the eddy viscosity coefficient is approximately equal to the eddy diffusion, as for most turbulent flows, the turbulent Prandtl number is close to one (Tennekes and Lumley 1972; Hinze 1975). We note, however, that some studies estimated the eddy viscosity coefficient based on mixing length arguments (Lemmin 1989; Jankowski and Catewicz 1984) and found it to be larger than the eddy diffusion coefficient (Lemmin 1989).

The estimated eddy diffusion of the island and no-island experiments are presented as a function of latitude in Fig. 12. These estimates are based on 10-day-resolution snapshots of the zonal velocity field and averaging over three years of simulation. We refrain from using longer averaging periods to avoid biases due to the equatorward migration of the zonal jets and the EMOC variability. The eddy diffusion coefficients vary mainly in the meridional direction and, to a lesser extent, in the vertical and zonal directions (not shown). The eddy coefficients are maximal in the vicinity of the jets, where the eddy generation and turbulent behavior is stronger. The global mean eddy diffusion coefficients are κ_h = 1700 and 760 $m^2 s^{-1}$ for the island and no-island experiments, respectively. For a basin size of some L = 5000 km, these values correspond to a typical basin-mixing time scale of $L^2/\kappa_h \approx 1000$ yr, not dramatically different from values one might expect for the present-day ocean. The estimated eddy diffusion coefficient is larger for the island case, most probably owing to the enhanced currents and enhanced variability near the island.

The eddy viscosity calculated here implies a EMOC cell width of about 1° (A13; A14), which is of the same order of the EMOC width observed in the actual eddy-resolving simulation here (Fig. 3) that does not rely on any prescribed eddy coefficients. This is another verification of both the scaling for the cell width presented in the above papers and of the eddy coefficient values presented here.

The spatiotemporal variability involved with the equatorward jet migration and EMOC oscillations also leads to mixing in our simulations, but this process is highly unisotropic and nonhomogeneous and cannot easily be represented using simple mixing arguments as above. Therefore, we merely note that the above mixing

coefficients are likely a lower bound on the effectiveness of mixing in the snowball ocean.

6. Summary and discussion

We studied snowball ocean dynamics at an eddy-resolving high resolution (1/8°) of a low-latitude ocean sector under "hard" snowball Earth conditions—that is, under an ice cover of about 1-km thickness and driven by a weak geothermal heat flux. Two configurations were considered, with and without a continent centered at the equator, motivated by the reconstructions indicating that continents were at low latitudes during the Neoproterozoic snowball Earth events. The temperature and salinity vary over small ranges and are uniform in the vertical direction over most regions as a result of convective mixing driven by geothermal heating. The oceanic dynamics in both configurations are highly turbulent, with zonal eddy-driven jets that show equatorward migration (Chan et al. 2007; Chemke and Kaspi 2015). The jets lead to enhanced coastal upwelling of deep water warmed by geothermal heating near the continent and, therefore, to strong ice-melting rates there. While these melting rates are an order of magnitude larger than both those estimated previously and atmospheric ice sublimation rates, they may not be sufficient to lead to open water and to explain the survival of photosynthetic life (Campbell et al. 2011; Tziperman et al. 2012). The equatorial meridional overturning circulation (EMOC) is restricted to very close to the equator and shows a strong variability in the form of relaxation oscillations that are especially strong in the no-island case, with a period of about 80 yr. These oscillations involve temperature and salinity changes that affect the stratification and lead to strong melt pulses that, in turn, affect the EMOC oscillations. Sensitivity experiments, supplementing the thorough coarse-resolution sensitivity studies of A14, indicate that the above features are robust, with the exception that the EMOC oscillations were suppressed for weak vertical diffusivity.

The driving of snowball circulation by bottom geothermal heating rather than by surface fluxes as in the present-day ocean is similar to the classical Rayleigh–Benard convection instead of "sideways convection" (Vallis 2006, section 15.2). The Rayleigh flux number (e.g., Boubnov and Golitsyn 1986) for a typical snowball ocean configuration is very large, indicating that one indeed expects the ocean to be vertically mixed by convection, as seen in our simulations that parameterize convection rather than resolving it.

The LEC and energy conversion rates between barotropic and baroclinic motions show that both barotropic and baroclinic mechanisms are responsible for eddy energy generation, while baroclinic instability seems the dominant eddy energy generation mechanism. The net kinetic energy conversion is from eddy to mean, owing to eddy–jet interactions, and as a result, the energy flow is from mean APE to eddy APE, to eddy kinetic energy, and then to mean kinetic energy. This is different from the energy flow in the present-day ocean where there are significant external sources of mean and eddy kinetic energy (von Storch et al. 2012), yet it is consistent with the present-day atmospheric LEC. The LEC discussed here is also similar to the energy cycle of baroclinic turbulence (e.g., Salmon 1980; Vallis 2006).

We estimated the eddy horizontal diffusion coefficient to be on the order of $1000\,m^2\,s^{-1}$. An estimate of the meridional width of the EMOC cell, using this eddy viscosity and the scaling of A13 and A14, is consistent with the EMOC width observed in our eddy-resolving calculations. This confirms both the eddy coefficient calculation and the estimates of the EMOC cell within the above papers.

Some readers may find the lack of specific observational constraints or motivation for the present study of eddies in a snowball ocean a significant concern. While we feel that the understanding of such a fascinating dynamical problem is its own reward, an interesting motivation was suggested to us by P. Hoffman (2014, personal communication). One candidate for refugia of photosynthetic life under hard snowball conditions is open water near geothermal vents and hotspots. Yet the lifetime of such geothermal vents and hotspots is shorter than the duration of snowball events. Photosynthetic bacteria or algae should therefore be effectively transported among such active geothermal sites, and this may happen in an energetic, eddying ocean but perhaps less so in a snowball ocean with no eddy motions. In addition, one cannot rule out, of course, the possibility that future geochemical proxies that depend on eddy diffusivity will be developed and find additional uses for this study.

The snowball ocean simulations presented here may be relevant to the dynamics of the oceans of icy moons such as Jupiter's moon Europa and Saturn's moon Enceladus (Vance and Goodman 2009), although we note some obvious caveats, including the very deep ocean of Europa (~100 km) relative to its radius, the much weaker Coriolis force, and the possible need to include commonly neglected components of the Coriolis force (Heimpel et al. 2005; Goodman 2012). Soderlund et al. (2014) recently studied the dynamics of Europa's ice-covered ocean and found a quasi-turbulent flow with two large EMOC cells that extend from the equator to

the midlatitudes, an extended equatorial zonal jet (extending to the midlatitudes), and opposite polar jets. These results are not consistent with the snowball ocean simulations presented here, and the origin of these differences requires further study.

The results presented here are restricted to the case of hard snowball Earth conditions with a constant (both spatially and temporally) prescribed ice depth. Further investigation of ocean circulation with open equatorial water ("soft" snowball), interactive ice-flow ocean dynamics, and a global domain will enrich our understanding of snowball Earth ocean dynamics, possibly of the initiation and termination of snowball events, and will also test our understanding of ocean dynamics in a different parameter regime.

Acknowledgments. This work was supported by NSF Grant AGS-1303604. We thank Rei Chemke, Hezi Gildor, Malte Jansen, Yohai Kaspi, and Martin Losch for helpful discussions. We thank G. Vallis and two anonymous reviewers for their most constructive and helpful suggestions. ET thanks the Weizmann Institute for its hospitality during parts of this work.

APPENDIX A

Lorenz Energy Cycle

We derive the equations for the LEC following Peixoto and Oort (1992) and von Storch et al. (2012). We first decompose the variables into a zonal mean represented by square brackets and deviations from the mean represented by a prime—for example, $u = [u] + u'$. Next, we multiply the zonal and meridional momentum equations by $[u]$ and $[v]$, correspondingly, apply a zonal mean, sum the two equations, use the hydrostatic equation, integrate over the entire ocean, multiply by ρ_0, use periodic boundary conditions in the zonal direction and zero flux at meridional boundaries, and use the condition of zero vertical velocity at the top and the bottom of the ocean. This leads to an equation for the kinetic energy of the mean flow K_M, and a similar procedure is used to derive one for the eddy kinetic energy K_E:

$$K_M = \frac{1}{2}\rho_0 \int ([u]^2 + [v]^2)\, dV \quad \text{and}$$
$$K_E = \frac{1}{2}\rho_0 \int ([u'^2] + [v'^2])\, dV. \tag{A1}$$

Next, we derive an equation for the APE of the mean flow and eddies by using the density equation, letting $\rho = [\rho] + \rho'$, multiplying the density equation by $[\rho]$, performing the zonal mean and multiplying by $g/\overline{\rho}_z$, where $\overline{\rho}$ is the average over time and horizontal dimensions, to find an equation for the mean APE and similarly for the eddy APE:

$$P_M = -\int \frac{g}{2\overline{\rho}_z}[\rho]^2\, dV \quad \text{and} \quad P_E = -\int \frac{g}{2\overline{\rho}_z}[\rho'^2]\, dV. \tag{A2}$$

The APE equations are further simplified by assuming that $\overline{\rho}_z$ slowly varies with depth so that its vertical derivative may be neglected. The sources of potential energy due to heating and melting at the bottom and the top of the ocean are found by vertically integrating the vertical diffusion term in the density equation and applying the top and bottom temperature and salinity boundary conditions using a linearized equation of state, giving a density boundary condition of the following form:

$$\kappa_v \rho_z = \alpha Q/c_p + \beta S_0 \phi, \tag{A3}$$

where α and β are the thermal and haline expansion coefficients, respectively, c_p is the heat capacity of ocean water, Q is the heat flux ($\mathrm{W\,m^{-2}}$), ϕ is the melting rate ($\mathrm{kg\,m^{-2}}$), and S_0 is the mean salinity.

The rate of change of the mean and eddy kinetic and potential energies are then

$$(K_M)_t = C(K_E, K_M) + C(P_M, K_M) + D(K_M), \tag{A4}$$
$$(K_E)_t = -C(K_E, K_M) + C(P_E, K_E) + D(K_E), \tag{A5}$$
$$(P_M)_t = -C(P_M, K_M) - C(P_M, K_E) + G(P_M) + D(P_M), \tag{A6}$$

and

$$(P_E)_t = -C(P_E, K_E) + C(P_M, K_E) + G(P_E) + D(P_E), \tag{A7}$$

In the above, the conversion terms are given by

$$C(K_E, K_M) = \rho_0 \int [u'\mathbf{v}'] \cdot \nabla[u]\, dV + \rho_0 \int [v'\mathbf{v}'] \cdot \nabla[v]\, dV, \tag{A8}$$

$$C(P_M, K_M) = -g \int [w][\rho]\, dV, \tag{A9}$$

$$C(P_E, K_E) = -g \int [w'\rho']\, dV, \quad \text{and} \tag{A10}$$

$$C(P_M, P_E) = \int \frac{g}{\overline{\rho}_z}[\mathbf{v}'\rho'] \cdot \nabla[\rho]\, dV, \tag{A11}$$

and the sources are given by

$$G(P_M) = -\int gL_x \left(\frac{\alpha[Q_s][\rho]|_{z=s}}{c_p \overline{\rho}_z|_{z=s}} - \frac{\alpha[Q_b][\rho]|_{z=b}}{c_p \overline{\rho}_z|_{z=b}} + \frac{\beta S_0[\phi_s][\rho]|_{z=s}}{\overline{\rho}_z|_{z=s}} \right) dy \quad \text{and} \tag{A12}$$

$$G(P_E) = -\int gL_x \left(\frac{\alpha[Q_s\rho']|_{z=s}}{c_p \overline{\rho}_z|_{z=s}} + \frac{\beta S_0[\phi_s\rho']|_{z=s}}{\overline{\rho}_z|_{z=s}} \right) dy, \tag{A13}$$

where subscripts s and b correspond to surface and bottom values. Following von Storch et al. (2012), the dissipation terms—$D(K_M)$, $D(K_E)$, $D(P_M)$, and $D(P_E)$—were calculated to close the balance of the energy equations. Given that our momentum dissipation involves a biharmonic Leith viscosity and the temperature and salinity equations involve spatially and temporally variable vertical diffusion coefficients, a direct estimation of the dissipation terms becomes nontrivial.

The conversion term $C(P_M, P_E)$ is typically associated with baroclinic instability. The kinetic energy conversion term may be written as a sum of horizontal and vertical components: $C(K_E, K_M) = C(K_E, K_M)_h + C(K_E, K_M)_v$, where the horizontal component $C(K_E, K_M)_h$ may be associated with barotropic instability or with the transfer of energy from eddies to the mean flows (zonal jets in our case), depending on the sign of the term. The vertical component $C(K_E, K_M)_v$ may be related to baroclinic instability. These are expressed as follows:

$$C(K_E, K_M)_h = \rho_0 \int [u'v'][u]_y \, dV + \rho_0 \int [v'^2][v]_y \, dV \quad \text{and} \tag{A14}$$

$$C(K_E, K_M)_v = \rho_0 \int [u'w'][u]_z \, dV + \rho_0 \int [v'w'][v]_z \, dV. \tag{A15}$$

In the present-day ocean, $C(K_E, K_M)_h \gg C(K_E, K_M)_v$ such that $C(K_E, K_M)$ is mostly associated with barotropic instability.

APPENDIX B

Transformation between the Barotropic and Baroclinic Modes of the Kinetic Energy

To calculate the energy transformation between barotropic and baroclinic modes of the kinetic energy, we have performed an analysis similar to that for the kinetic energy of the mean flow discussed above, but now considering the vertical mean (represented by the brackets) instead of the zonal mean. The barotropic and baroclinic energies are defined as follows:

$$K_{\text{bt}} = \frac{\rho_0}{2} \int ([u]^2 + [v]^2) \, dV \quad \text{and} \tag{B1}$$

$$K_{\text{bc}} = \frac{\rho_0}{2} \int ([u'^2] + [v'^2]) \, dV, \tag{B2}$$

and their equations are

$$(K_{\text{bt}})_t = C(K_{\text{bc}}, K_{\text{bt}}) + D(K_{\text{bt}}) \quad \text{and} \tag{B3}$$

$$(K_{\text{bc}})_t = -C(K_{\text{bc}}, K_{\text{bt}}) + D(K_{\text{bc}}), \tag{B4}$$

where

$$C(K_{\text{bc}}, K_{\text{bt}}) = \rho_0 H \int [u'\mathbf{v}'] \cdot \nabla[u] \, dx \, dy + \rho_0 H \int [v'\mathbf{v}'] \cdot \nabla[v] \, dx \, dy, \tag{B5}$$

and

$$D(K_{\text{bt}}) = \rho_0 H \int ([u][F_u] + [v][F_v]) \, dx \, dy \quad \text{and} \tag{B6}$$

$$D(K_{\text{bc}}) = \rho_0 \int ([u'F_u] + [v'F_v]) \, dV. \tag{B7}$$

In the above equations, H is the ocean depth, and F_u and F_v are the zonal and meridional viscosity terms, respectively.

APPENDIX C

Back-of-the-Envelope Estimate of the Available Potential Energy

As a useful verification of the LEC analysis, we estimate the APE of a snowball-like ocean motivated by our numerical results. We consider an ocean with the density linearly varying in the meridional direction and uniform in the vertical direction, given by $\rho(y) = \rho_0 + \overline{\rho}_y(y - L_y/2)$, where ρ_0 is the mean ocean density, $\overline{\rho}_y$ (=constant) is the meridional density gradient, and L_y is the meridional extent of the domain. The potential energy of this setup is

$$P_2 = gL_x \int_0^{L_y} \int_{-H}^{0} \rho(y) z \, dz \, dy = -gL_x L_y \rho_0 \frac{H^2}{2}, \tag{C1}$$

where L_x is the zonal extent of the domain, and H is the ocean depth. We define the APE as the potential energy

of the ocean state minus the minimal energy of the ocean under adiabatic redistribution of the mass. Such minimal potential energy is obtained when the ocean is vertically stratified: $\rho(z) = \rho_0 + \overline{\rho}_z(y + H/2)$, where we let $\overline{\rho}_z = \overline{\rho}_y L_y/H$ reflect an adiabatic redistribution of the ocean density. The minimum potential energy is then

$$P_1 = gL_xL_y\left(\frac{1}{12}\overline{\rho}_z H^3 - \frac{1}{2}\rho_0 H^2\right), \qquad \text{(C2)}$$

and the APE is

$$P_2 - P_1 = -\frac{1}{12}gL_xL_y\overline{\rho}_z H^3 = -\frac{1}{12}gL_xL_y^2\overline{\rho}_y H^2, \qquad \text{(C3)}$$

where $L_x = 4.9 \times 10^6$ m, $L_y = 4.6 \times 10^6$ m, $H = 2000$ m, and $\overline{\rho}_y = 2 \times 10^{-8}\,\mathrm{kg\,m^{-4}}$. Using these typical values for our model setup, the APE is 6.8 EJ. This value is equivalent to 0.2 ZJ when multiplying by the ratio between the present-day ocean volume and the equatorial sector ocean volume of the simulations. This estimate is, reassuringly, on the same order of (more precisely, 36% of) the APE of the mean flow shown in Fig. 10.

REFERENCES

Abbot, D., A. Voigt, and D. Koll, 2011: The Jormungand global climate state and implications for Neoproterozoic glaciations. *J. Geophys. Res.*, **116**, D18103, doi:10.1029/2011JD015927.

Adcroft, A., J. R. Scott, and J. Marotzke, 2001: Impact of geothermal heating on the global ocean circulation. *Geophys. Res. Lett.*, **28**, 1735–1738, doi:10.1029/2000GL012182.

——, and Coauthors, 2010: MITgcm user manual. [Available online at http://mitgcm.org/public/r2_manual/latest/online_documents/manual.html.]

Ashkenazy, Y., H. Gildor, M. Losch, F. A. Macdonald, D. P. Schrag, and E. Tziperman, 2013: Dynamics of a snowball Earth ocean. *Nature*, **495**, 90–93, doi:10.1038/nature11894.

——, ——, ——, and E. Tziperman, 2014: Ocean circulation under globally glaciated snowball Earth conditions: Steady state solutions. *J. Phys. Oceanogr.*, **44**, 24–43, doi:10.1175/JPO-D-13-086.1.

Boubnov, B., and G. Golitsyn, 1986: Experimental study of convective structures in rotating fluids. *J. Fluid Mech.*, **167**, 503–531, doi:10.1017/S002211208600294X.

Campbell, A. J., E. D. Waddington, and S. G. Warren, 2011: Refugium for surface life on snowball Earth in a nearly-enclosed sea? A first simple model for sea-glacier invasion. *Geophys. Res. Lett.*, **38**, L19502, doi:10.1029/2011GL048846.

Chan, C. J., R. A. Plumb, and I. Cerovecki, 2007: Annular modes in a multiple migrating zonal jet regime. *J. Atmos. Sci.*, **64**, 4053–4068, doi:10.1175/2007JAS2156.1.

Chemke, R., and Y. Kaspi, 2015: Poleward migration of eddy-driven jets. *J. Adv. Model. Earth Syst.*, **7**, 1457–1471, doi:10.1002/2015MS000481.

Christie-Blick, N., L. E. Sohl, and M. J. Kennedy, 1999: Considering a Neoproterozoic snowball Earth. *Science*, **284**, 1087, doi:10.1126/science.284.5417.1087a.

Farrell, B. F., and P. J. Ioannou, 1995: Stochastic dynamics of the midlatitude atmospheric jet. *J. Atmos. Sci.*, **52**, 1642–1656, doi:10.1175/1520-0469(1995)052<1642:SDOTMA>2.0.CO;2.

——, and ——, 2003: Structural stability of turbulent jets. *J. Atmos. Sci.*, **60**, 2101–2118, doi:10.1175/1520-0469(2003)060<2101:SSOTJ>2.0.CO;2.

Ferreira, D., J. Marshall, and B. E. J. Rose, 2011: Climate determinism revisited: Multiple equilibria in a complex climate model. *J. Climate*, **24**, 992–1012, doi:10.1175/2010JCLI3580.1.

Gargett, A., 1984: Vertical eddy diffusivity in the ocean interior. *J. Mar. Res.*, **42**, 359–393, doi:10.1357/002224084788502756.

Goodman, J. C., 2006: Through thick and thin: Marine and meteoric ice in a "snowball Earth" climate. *Geophys. Res. Lett.*, **33**, L16701, doi:10.1029/2006GL026840.

——, 2012: Tilted geostrophic convection in icy world oceans caused by the horizontal component of the planetary rotation vector. *2012 Fall Meeting*, San Francisco, CA, Amer. Geophys. Union, Abstract P51A–2017.

——, and R. T. Pierrehumbert, 2003: Glacial flow of floating marine ice in "snowball Earth." *J. Geophys. Res.*, **108**, 3308, doi:10.1029/2002JC001471.

Harland, W. B., 1964: Evidence of late Precambrian glaciation and its significance. *Problems in Palaeoclimatology*, A. E. M. Nairn, Ed., John Wiley and Sons, 119–149, 180–184.

Heimpel, M. H., J. M. Aurnou, F. M. Al-Shamali, and N. Gomez Perez, 2005: A numerical study of dynamo action as a function of spherical shell geometry. *Earth Planet. Sci. Lett.*, **236**, 542–557, doi:10.1016/j.epsl.2005.04.032.

Hinze, J. O., 1975: *Turbulence*. McGraw-Hill, 790 pp.

Hoffman, P., and D. Schrag, 2002: The snowball Earth hypothesis: Testing the limits of global change. *Terra Nova*, **14**, 129–155, doi:10.1046/j.1365-3121.2002.00408.x.

——, A. J. Kaufman, G. P. Halverson, and D. P. Schrag, 1998: A Neoproterozoic snowball Earth. *Science*, **281**, 1342–1346, doi:10.1126/science.281.5381.1342.

Huang, R. X., 1999: Mixing and energetics of the oceanic thermohaline circulation. *J. Phys. Oceanogr.*, **29**, 727–746, doi:10.1175/1520-0485(1999)029<0727:MAEOTO>2.0.CO;2.

Jackett, D. R., and T. J. McDougall, 1995: Minimal adjustment of hydrographic profiles to achieve static stability. *J. Atmos. Oceanic Technol.*, **12**, 381–389, doi:10.1175/1520-0426(1995)012<0381:MAOHPT>2.0.CO;2.

Jankowski, A., and Z. Catewicz, 1984: Characteristics of horizontal macroturbulence due to the currents in the Baltic Sea. *Dtsch. Hydrogr. Z.*, **37**, 173–200, doi:10.1007/BF02226971.

Jansen, M., and R. Ferrari, 2012: Macroturbulent equilibration in a thermally forced primitive equation system. *J. Atmos. Sci.*, **69**, 695–713, doi:10.1175/JAS-D-11-041.1.

Kennedy, M. J., N. Christie-Blick, and L. E. Sohl, 2001: Are Proterozoic cap carbonates and isotopic excursions a record of gas hydrate destabilization following Earth's coldest intervals? *Geology*, **29**, 443–446, doi:10.1130/0091-7613(2001)029<0443:APCCAI>2.0.CO;2.

——, ——, and ——, 2002: Reply to "Are Proterozoic cap carbonates and isotopic excursions a record of gas hydrate destabilization following Earth's coldest intervals?" *Geology*, **30**, 763, doi:10.1130/0091-7613(2002)030<0763:>2.0.CO;2.

Kirschvink, J. L., 1992: Late Proterozoic low-latitude glaciation: The snowball Earth. *The Proterozoic Biosphere*, J. W. Schopf and C. Klein, Eds., Cambridge University Press, 51–52.

Ledwell, J. R., A. J. Watson, and C. S. Law, 1993: Evidence for slow mixing across the pycnocline from an open ocean tracer release experiment. *Nature*, **364**, 701–703, doi:10.1038/364701a0.

Le-Hir, G., G. Ramstein, Y. Donnadieu, and R. T. Pierrehumbert, 2007: Investigating plausible mechanisms to trigger a deglaciation from a hard snowball Earth. *C. R. Geosci.*, **339**, 274–287, doi:10.1016/j.crte.2006.09.002.

Leith, C. E., 1967: Diffusion approximation to inertial energy transfer in isotropic turbulence. *Phys. Fluids*, **10**, 1409–1416, doi:10.1063/1.1762300.

——, 1996: Stochastic models of chaotic systems. *Physica D*, **98**, 481–491, doi:10.1016/0167-2789(96)00107-8.

Lemmin, U., 1989: Dynamics of horizontal turbulent mixing in a nearshore zone of Lake Geneva. *Limnol. Oceanogr.*, **34**, 420–434, doi:10.4319/lo.1989.34.2.0420.

Li, D., and R. T. Pierrehumbert, 2011: Sea glacier flow and dust transport on snowball Earth. *Geophys. Res. Lett.*, **38**, L17501, doi:10.1029/2011GL048991.

Li, L., A. P. Ingersoll, X. Jiang, D. Feldman, and Y. L. Yung, 2007: Lorenz energy cycle of the global atmosphere based on reanalysis datasets. *Geophys. Res. Lett.*, **34**, L16813, doi:10.1029/2007GL029985.

Li, Z. X., and Coauthors, 2008: Assembly, configuration, and break-up history of Rodinia: A synthesis. *Precambrian Res.*, **160**, 179–210, doi:10.1016/j.precamres.2007.04.021.

Lorenz, E. N., 1955: Available potential energy and the maintenance of the general circulation. *Tellus*, **7A**, 157–167, doi:10.1111/j.2153-3490.1955.tb01148.x.

Losch, M., 2008: Modeling ice shelf cavities in a z coordinate ocean general circulation model. *J. Geophys. Res.*, **113**, C08043, doi:10.1029/2007JC004368.

Lubick, N., 2002: Palaeoclimatology: Snowball fights. *Nature*, **417**, 12–13, doi:10.1038/417012a.

Marotzke, J., and M. Botzet, 2007: Present-day and ice-covered equilibrium states in a comprehensive climate model. *Geophys. Res. Lett.*, **34**, L16704, doi:10.1029/2006GL028880.

Marshall, J., A. Adcroft, C. Hill, L. Perelman, and C. Heisey, 1997: A finite-volume, incompressible Navier Stokes model for studies of the ocean on parallel computers. *J. Geophys. Res.*, **102**, 5753–5766, doi:10.1029/96JC02775.

Mashayek, A., R. Ferrari, G. Vettoretti, and W. R. Peltier, 2013: The role of the geothermal heat flux in driving the abyssal ocean circulation. *Geophys. Res. Lett.*, **40**, 3144–3149, doi:10.1002/grl.50640.

Munk, W., and C. Wunsch, 1998: Abyssal recipes II: Energetics of tidal and wind mixing. *Deep-Sea Res. I*, **45**, 1977–2010, doi:10.1016/S0967-0637(98)00070-3.

Oort, A. H., and J. P. Peixoto, 1983: Global angular momentum and energy balance requirements from observations. *Adv. Geophys.*, **25**, 355–490, doi:10.1016/S0065-2687(08)60177-6.

Peixoto, J., and A. Oort, 1992: *Physics of Climate.* American Institute of Physics, 520 pp.

Pierrehumbert, R. T., D. S. Abbot, A. Voigt, and D. Koll, 2011: Climate of the Neoproterozoic. *Annu. Rev. Earth Planet. Sci.*, **39**, 417–460, doi:10.1146/annurev-earth-040809-152447.

Pollack, H., S. Hurter, and J. Johnson, 1993: Heat flow from the earth's interior: Analysis of the global data set. *Rev. Geophys.*, **31**, 267–280, doi:10.1029/93RG01249.

Pollard, D., and J. F. Kasting, 2005: Snowball Earth: A thin-ice solution with flowing sea glaciers. *J. Geophys. Res.*, **110**, C07010, doi:10.1029/2004JC002525.

Poulsen, C. J., and R. L. Jacob, 2004: Factors that inhibit snowball Earth simulation. *Paleoceanography*, **19**, PA4021, doi:10.1029/2004PA001056.

——, R. T. Pierrehumbert, and R. L. Jacob, 2001: Impact of ocean dynamics on the simulation of the Neoproterozoic "snowball Earth." *Geophys. Res. Lett.*, **28**, 1575–1578, doi:10.1029/2000GL012058.

——, R. L. Jacob, R. T. Pierrehumbert, and T. T. Huynh, 2002: Testing paleogeographic controls on a Neoproterozoic snowball Earth. *Geophys. Res. Lett.*, **29**, 1515, doi:10.1029/2001GL014352.

Rhines, P. B., 1979: Geostrophic turbulence. *Annu. Rev. Fluid Mech.*, **11**, 401–441, doi:10.1146/annurev.fl.11.010179.002153.

Salmon, R., 1980: Baroclinic instability and geostrophic turbulence. *Geophys. Astrophys. Fluid Dyn.*, **15**, 167–211, doi:10.1080/03091928008241178.

Schrag, D. P., and P. F. Hoffman, 2001: Geophysics: Life, geology and snowball Earth. *Nature*, **409**, 306, doi:10.1038/35053170.

Scott, J. R., J. Marotzke, and A. Adcroft, 2001: Geothermal heating and its influence on the meridional overturning circulation. *J. Geophys. Res.*, **106**, 31 141–31 154, doi:10.1029/2000JC000532.

Soderlund, K. M., B. E. Schmidt, J. Wicht, and D. D. Blankenship, 2014: Ocean-driven heating of Europa's icy shell at low latitudes. *Nat. Geosci.*, **7**, 16–19, doi:10.1038/ngeo2021.

Sohl, L. E., and M. A. Chandler, 2007: Reconstructing Neoproterozoic palaeoclimates using a combined data/modelling approach. *Deep-Time Perspectives on Climate Change: Marrying the Signal from Computer Models and Biological Proxies*, M. M. Williams et al., Eds., Geological Society, 61–80.

Tennekes, H., and J. L. Lumley, 1972: *A First Course in Turbulence.* The MIT Press, 300 pp.

Tziperman, E., D. S. Abbot, Y. Ashkenazy, H. Gildor, D. Pollard, C. Schoof, and D. P. Schrag, 2012: Continental constriction and oceanic ice-cover thickness in a snowball-Earth scenario. *J. Geophys. Res.*, **117**, C05016, doi:10.1029/2011JC007730.

Vallis, G. K., 2006: *Atmospheric and Oceanic Fluid Dynamics.* Cambridge University Press, 745 pp.

Vance, S., and J. M. Brown, 2005: Layering and double-diffusion style convection in Europa's ocean. *Icarus*, **177**, 506–514, doi:10.1016/j.icarus.2005.06.005.

——, and J. Goodman, 2009: Oceanography of an ice-covered moon. *Europa*, R. T. Pappalardo, W. B. McKinnon, and K. K. Khurana, Eds., University of Arizona Press, 459–482.

von Storch, J. S., C. Eden, I. Fast, H. Haak, D. Hernández-Deckers, E. Maier-Reimer, J. Marotzke, and D. Stammer, 2012: An estimate of the Lorenz energy cycle for the world ocean based on the 1/10° STORM/NCEP simulation. *J. Phys. Oceanogr.*, **42**, 2185–2205, doi:10.1175/JPO-D-12-079.1.

Wunsch, C., and R. Ferrari, 2004: Vertical mixing, energy, and the general circulation of the oceans. *Annu. Rev. Fluid Mech.*, **36**, 281–314, doi:10.1146/annurev.fluid.36.050802.122121.